

Reconstruction of the Structure of Accretion Disks in Dwarf Novae from the Multi-Band Light Curves of Early Superhumps

Makoto UEMURA

Hiroshima Astrophysical Science Center, Hiroshima University, Kagamiyama 1-3-1, Higashi-Hiroshima, Hiroshima 739-8526
uemuram@hiroshima-u.ac.jp

Taichi KATO, Tomohito OHSHIMA

Department of Astronomy, Kyoto University, Kitashirakawa-Oiwake-cho, Sakyo-ku, Kyoto 606-8502
and

Hiroyuki MAEHARA

Kwasan and Hida Observatories, Kyoto University, Yamashina-ku, Kyoto 607-8471

(Received 2011 December 27; accepted 2012 March 6)

Abstract

We propose a new method to reconstruct the structure of accretion disks in dwarf novae using multi-band light curves of early superhumps. Our model assumes that early superhumps are caused by the rotation effect of non-axisymmetrically flaring disks. We have developed a Bayesian model for this reconstruction, in which a smoother disk-structure tends to have a higher prior probability. We analyzed simultaneous optical and near-infrared photometric data of early superhumps of the dwarf nova, V455 And using this technique. The reconstructed disk has two flaring parts in the outermost region of the disk. These parts are responsible for the primary and secondary maxima of the light curves. The height-to-radius ratio is $h/r = 0.20\text{--}0.25$ in the outermost region. In addition to the outermost flaring structures, flaring arm-like patterns can be seen in an inner region of the reconstructed disk. The overall profile of the reconstructed disk is reminiscent of the disk structure that is deformed by the tidal effect. However, an inner arm-like pattern, which is responsible for the secondary minimum in the light curve, cannot be reproduced only by the tidal effect. It implies the presence of another mechanism that deforms the disk structure. Alternatively, the temperature distribution of the disk could be non-axisymmetric. We demonstrate that the disk structure with weaker arm-like patterns is optimal in the model including the irradiation effect. However, the strongly irradiated disk gives quite blue colors, which may conflict with the observation. Our results suggest that the amplitude of early superhumps depends mainly on the height of the outermost flaring regions of the disk. We predict that early superhumps can be detected with an amplitude of > 0.02 mag in about 90 % of WZ Sge stars.

Key words: accretion, accretion disks — stars: dwarf novae

1. Introduction

Early superhumps are periodic variations occasionally observed in WZ Sge-type dwarf novae in their superoutbursts (Kato et al. 1996). Their period is extremely close to the orbital period of the binary system. Their light curve has a double-peaked profile with different amplitudes. These characteristics of early superhumps suggest that they are caused by a different mechanism from that of ordinary superhumps, which are commonly observed in all SU UMa-type dwarf novae; the period of ordinary superhumps is a few percent longer than the orbital period, and the light curve generally has a saw-tooth profile with a prominent single peak (Vogt 1980; Warner 1985; for a recent review, see Kato et al. 2009). The amplitude of early superhumps is $\lesssim 0.5$ mag, and is largest at the superoutburst maximum. Then, early superhumps decreases in amplitude with time, and finally, ordinary superhumps supersede early superhumps ~ 10 d after the superoutburst maximum (Ishioaka et al. 2002; Kato 2002). Thus, early superhumps are observed only in the early stage of

superoutbursts of WZ Sge stars.

The mechanism of early superhumps is poorly understood. In contrast, the mechanism of ordinary superhumps have been understood in terms of the tidal dissipation in eccentric, precessing accretion-disks. A disk in a binary system is theoretically expected to have an eccentric form when it expands beyond the 3:1 resonance radius (Whitehurst 1988; Lubow 1991). In the case of WZ Sge stars, the disk possibly expands far beyond the 3:1 resonance radius. This is due to their extreme mass-ratios ($M_2/M_1 \lesssim 0.1$, where M_2 and M_1 denote the secondary and primary masses), and the lack of normal outbursts; thereby, a large amount of matter is expected to be stored before superoutbursts (Osaki 1995). Hence, early superhumps are probably variations occurring in such a large disk, which definitely shows strong tidal distortion.

An important feature of early superhumps is a large variety of their amplitudes; it is larger than 0.4 mag in some objects, while it is smaller than 0.1 mag, or not significantly detected, in other objects (e.g., Kato 2002). In particular, edge-on (or a high inclination) systems tend to ex-

hibit large amplitudes of early superhumps. This feature suggests that early superhumps can be attributed to the rotation effect of a disk that has a non-axisymmetric vertical structure (Nogami et al. 1997). Maehara et al. (2007) reproduce the light curve of early superhumps in BC UMa, assuming asymmetric spiral-patterns in the disk.

Osaki, Meyer (2002) propose that early superhumps are caused by a two-armed spiral pattern that is generated by the 2:1 resonance. In their model, the observed amplitude can be explained when the geometrical effect of disks is considered, that is, the vertical expansion along the spiral pattern. SPH simulations have shown the appearance of the two-armed spiral pattern at the 2:1 resonance radius (Kunze 2004; Kunze, Speith 2005). A non-axisymmetrically expanded structure can be expected even without the resonance (Smak 2001; Ogilvie 2002). Kato (2002) propose that early superhumps can be interpreted as irradiated emission of the elevated surface of the disk caused by the vertical tidal deformation. In order to evaluate those models, detailed observations have been long awaited for early superhumps.

Most recently, Matsui et al. (2009) (Paper I) succeeded in measuring the color variations associated with early superhumps for the first time. In Paper I, multi-band photometric observations during the superoutburst of V455 And were reported. The observations revealed that the hump component was redder than the stationary component. Paper I suggest that the source of early superhumps is a vertically-expanded low-temperature region, probably located in an outer part of the disk. In addition, it is interesting that the phase at which the object was reddest significantly shifted to the phase of the flux maximum. If the vertically-expanded region is limited at the outermost region, the flux maximum coincides with the reddest phase. The observed phase shift implies that a part of the vertically-expanded region is located not in the outermost part, but in a relatively inner part of the disks.

The idea of the reconstruction of the geometrical structure of disks is then motivated by the color behavior of early superhumps in V455 And. The phase of the humps would have information about the azimuthal structure of the disk, while the color of the humps would have information about the radial structure. Therefore, the height of each point in the disk could, in principle, be reconstructed using multi-band light curves of early superhumps. It is well known that the intensity map of the disk in dwarf novae can be reconstructed by using a tomography technique; the eclipse mapping uses the light curves of eclipses (Horne 1985), and Doppler tomography uses variations in emission-line profiles (Marsh, Horne 1988). In addition to these methods, we propose a new tomography method to reconstruct the height map of disks using early superhumps, which we call the “early superhump mapping”.

In this paper, we present our model for early-superhump mapping that is based on a Bayesian technique. The model is described in the next section. We also present demonstrations of early superhump mapping using artificial data sets in this section. In section 3, we use this method for the light curves of V455 And. We dis-

cuss the dependence based on assumed parameters in the model and the temporal evolution of the reconstructed disk-structures. In section 4, the effect of irradiation is evaluated. We also discuss the physical implication obtained from the reconstructed disk-structure. Finally, we summarize our findings in section 5.

2. Model

We consider a disk with a height map, $\{h(r, \theta)\}$, where r and θ is radial and azimuthal components in the cylindrical coordinate system whose origin is located at the disk center; $r = \sqrt{x^2 + y^2}$ and $\tan \theta = y/x$ ($0 \leq \theta < 2\pi$). We take the x -axis in the direction of the center of the secondary star, and the y -axis in the direction of the motion of the secondary. The center of the secondary star is located at $(x, y) = (1.0, 0.0)$, and the binary separation is set to be $a = 1.0$. Hence, $h = h/a$ in this paper.

Our model assumes that all emission that we observe is that from the disk surface defined with $\{h\}$. Then, the observed flux density, $f_\nu(\phi)$, at a given frequency, ν , and a given phase, ϕ can be described as a function of the inclination angle, i and $\{h\}$. We develop a model to estimate $\{h\}$ from $f_\nu(\phi)$, assuming i . The reconstruction of $\{h\}$ is not only an inverse problem, but also a non-linear problem, because a part of the disk could be occulted by the other parts of the disk or by the secondary star. We approach this problem with a Bayesian framework. Our Bayesian model estimates the posterior distribution of $\{h\}$ by using the Markov chain Monte Carlo (MCMC) method.

2.1. Geometry and Emission from the Disk

We calculate the flux from the disk at each phase using a similar method reported in Hachisu, Kato (2001). The disk surface is divided into small patches. A patch is defined as a closed region bounded by four segments of grid lines. In the azimuth direction, the grids divide the disk into N_θ equally-spaced bins. In the radial direction, the disk is divided into N_r bins between the inner radius, r_{in} and the outer radius, r_{out} . The width of the radial bin is equally-spaced in a logarithmic scale; the i -th coordinate in r is described as $\log_{10}(r_i/r_{\text{in}}) = \log_{10}(r_{\text{out}}/r_{\text{in}}) \times i/N_r$. The center position, area, and normal vector of each patch are defined as the same manner as described in Hachisu, Kato (2001).

Each patch emits blackbody radiation with a temperature of T at the center of the patch. We assume the following temperature distribution of the standard accretion disk model (Shakura, Syunyaev 1973);

$$T = T_{\text{in}} \left(\frac{r}{r_{\text{in}}} \right)^{-3/4}, \quad (1)$$

where T_{in} is the temperature at the innermost part of the disk. The flux from each patch can be calculated from T , the size and normal vector of the patch, and a viewing angle defined by ϕ and i . The flux in a given photometric band is calculated as the flux density of the blackbody radiation at the center wavelength of the band. We used g , V , R_c , I_c , and J bands, and their center wavelengths were

set to be 0.4858, 0.5505, 0.6588, 0.8060, and 1.2150 μm , respectively.

The total flux at a given phase is a sum of the flux from all visible patches in the viewing direction corresponding to the phase. We consider the self-occultation in the disk; that is, the flux from the patch is not counted if the center of a patch is occulted by the other patch. In addition, the eclipse of the disk by the secondary star is also considered. The flux from a patch is counted if the patch center is outside the Roche-lobe area projected perpendicular to the viewing direction. We neglect the emission from the white dwarf (WD) and boundary layer. They mainly contribute to the high energy emission from an inner region, and less contribute to the emission from an outer region where the early superhump originates. Thus, we calculate multi-band light-curves, $f_\nu(\phi)$ from a set of $h(r, \theta)$. The model light-curves are normalized by the average flux for each band in order to be compared with the observed light-curves.

2.2. Bayesian Model

In general, a Bayesian approach provides a means for estimating the posterior probability distribution of model parameters from the likelihood function and prior probability distribution. Our Bayesian model estimates the posterior probability of $\{h(r, \theta)\}$, $P(h)$. The model can be expressed as follows:

$$P(h) = cL(f_{\nu, \text{obs}}, f_{\nu, \text{model}})\pi(h), \quad (2)$$

where L is the likelihood function and π is the prior distribution. The normalization factor, c is not important for estimating $P(h)$ by using the MCMC method.

The likelihood function, L , is defined with the observed and model light curves for each band. The model light curve is derived from a given $\{h\}$, as described in the last subsection. The model assumes that the observed fluxes have a Gaussian distribution with a mean of the model fluxes and a variance of σ^2 . Here, σ corresponds to photometric errors of the observed light curve. Hence, L is expressed as;

$$L = \prod_{i,j} \frac{1}{\sqrt{2\pi\sigma_{i,j}^2}} \exp\left(-\frac{[f_{\nu_i, \text{obs}}(\phi_j) - f_{\nu_i, \text{model}}(\phi_j)]^2}{2\sigma_{i,j}^2}\right), \quad (3)$$

where the subscripts i and j denote the band and phase, respectively.

The prior distribution, π , is a function of $\{h\}$, and essential to solve the present inverse problem. The prior probability distribution in our model consists of two components. The first one is for the smoothness of the disk structure. It has a form:

$$\pi_{\text{smooth}} = \frac{1}{\sqrt{2\pi w^2}} \prod_{l,m} \left[\exp\left(-\frac{[h_{l,m} - 2h_{l-1,m} + h_{l-2,m}]^2}{2w^2}\right) \exp\left(-\frac{[h_{l,m} - 2h_{l,m-1} + h_{l,m-2}]^2}{2w^2}\right) \right], \quad (4)$$

where $h_{l,m}$ denote the l -th and m -th grid points in the

radial and azimuthal directions, namely, $h_{l,m} = h(r_l, \theta_m)$ ($l = 1, \dots, N_r + 1$ and $m = 1, \dots, N_\theta$). This prior distribution means that a sequence of the second difference of $\{h_{l,m}\}$ in the radial and azimuthal directions follows a normal distribution having a standard deviation of w . A smoother height-structure provides a higher π_{smooth} . The weight parameter w plays a role in adjusting the smoothness of estimated disk-structures.

The second prior distribution provides a default map of $\{h_{l,m}\}$. It is widely accepted that the emission of outbursting dwarf-novae can be explained by the standard-disk model (Shakura, Syunyaev 1973). In this model, viscous heating in the disk is balanced by cooling by blackbody radiation from the disk surface. Its vertical structure is determined by hydrostatic equilibrium. The disk height is expected to be proportional to the radius in this scheme. In our model, we define, $h_{\text{disk}} = 0.1r$, and the prior distribution, π_{disk} as a product of truncated normal distributions with means and standard deviations of h_{disk} :

$$\pi_{\text{disk}} = \begin{cases} \prod_{l,m} \frac{1}{\sqrt{2\pi h_{\text{disk},l,m}^2}} \exp\left(-\frac{[h_{l,m} - h_{\text{disk},l,m}]^2}{2h_{\text{disk},l,m}^2}\right) & (h_{l,m} \geq 0) \\ 0 & (h_{l,m} < 0). \end{cases} \quad (5)$$

This prior distribution is useful to reject a height map containing too large h , which violates the assumption of the standard-disk model that the disk is geometrically thin. The assumed h_{disk} could be much larger than those expected in the standard disk of dwarf novae. According to Kato et al. (2008), the disk height is estimated to be $h/r \sim c_s/r\Omega_K$, where c_s and Ω_K denote the sound speed and Keplerian angular speed at distance r , respectively. For typical parameters of dwarf novae ($T = 10^4$ K, $r_{\text{out}} = 10^{10}$ cm, and $M_{\text{WD}} = 0.6M_\odot$), it gives $h \sim 0.01r$. This is one order smaller than that we assumed. However, we consider accretion disks that could be deformed by a strong tidal effect. In such a condition, the hydrostatic balance definitely changes, and thereby the expected height-map could also change. Therefore, π_{disk} defined in equation (5) is a reasonable choice as a default map. The prior distribution of our model is, in total, expressed as $\pi = \pi_{\text{smooth}} \pi_{\text{disk}}$.

Taken together, we estimate $P(h_{l,m})$ having $N_h = N_\theta(N_r + 1)$ elements (including disk edges), using $N_{\text{data}} = N_i N_j$ photometric data. The means of $P(h_{l,m})$ give $h_{l,m}$. We estimate $P(h_{l,m})$ using a MCMC algorithm. In Appendix, we present a detailed description of our MCMC calculation. In the present work, we used $\sigma_{i,j} = 0.01$ mag, $N_\theta = 20$, $N_r = 16$, and $w = 1.0$. A larger number of grids makes the amount of calculation significantly larger and the convergence slower. The above values of N_θ and N_r are the allowable maximum ones in terms of the calculation time. The parameters σ and w correspond to the weights of the likelihood and prior distribution components. A small value of σ/w leads to a slow convergence. In the present model, all of those parameters (σ , N_θ , N_r , and w) are related to a kind of ‘‘resolution’’ of reconstructed images. Examples for different values of those parameters are given in Appendix.

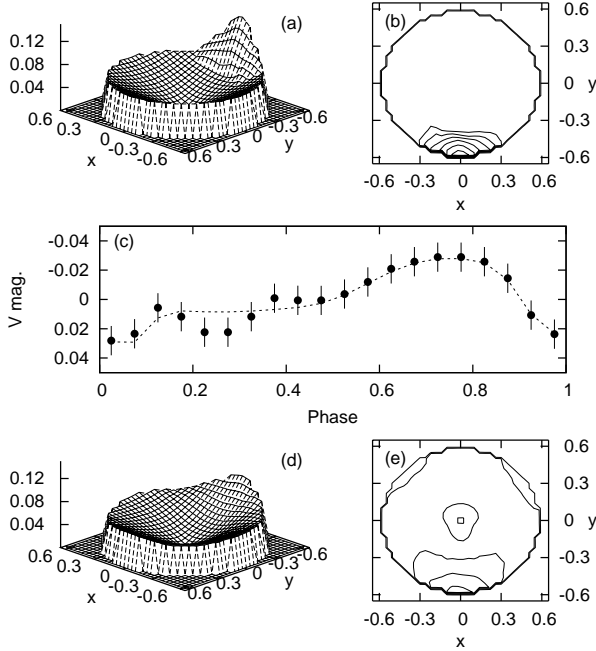


Fig. 1. Demonstration of the early superhump mapping for case 1. Panel (a): assumed disk structure. Panel (b): contour of the height ratio, h/r . Panel (c): V -band light curve. The filled circles and dashed line represent the artificial data and model light curve, respectively. Panels (d) and (e): the same as (a) and (b), but for the reconstructed disk structure. The center of the secondary star is located at $(x, y) = (1.0, 0.0)$ in panels (a), (b), (d), and (e). Panels (b) and (d) show contours of $h/r = 0.07$ – 0.21 with an interval of 0.02 . The height maps are shown by linear interpolations of the original height grids, $\{h(r_l, \theta_m)\}$ ($l = 1, \dots, N_r + 1$, $m = 1, \dots, N_\theta$).

2.3. Demonstration with Artificial Data

In this subsection, we present several demonstrations of our early superhump mapping using artificial data sets. Figure 1, 2, and 3 show three sets of artificial data and results of the early superhump mapping, which we call cases 1, 2, and 3, respectively. In all three cases, non-axisymmetrically flaring regions are assumed to be superimposed on a disk having $h_{\text{disk}} = 0.1r$. In those figures, panel (a) depicts the assumed disk structure. Panel (b) shows contours of the height ratio, h/r . Non-axisymmetric features can be seen more conspicuously in panel (b). The light curves of the g , V , R_c , I_c , and J -bands were calculated by “observations” of those disks, as described in the last subsection. The V -band light curves are shown in panel (c), as indicated by the filled circles. We assumed a photometric error of 0.01 mag in all bands and phases. The dashed lines denote the model light curves. Phase 0 is defined as the time of the mid-eclipse. Panels (d) and (e) are the same as (a) and (b), but for the reconstructed height map. The model parameters are listed in table 1.

In case 1, the disk has a flaring part in the outermost region of the disk. The peak height is 0.14 ($h/r = 0.23$). In case 2, the disk has a flaring part in a relatively inner

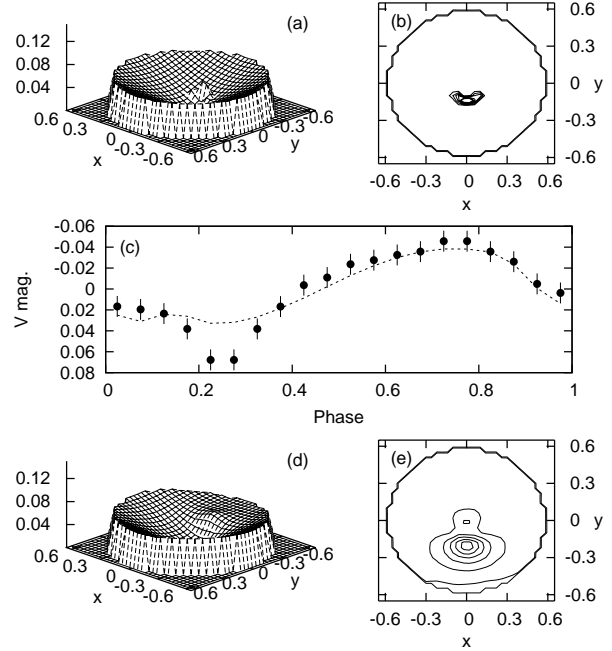


Fig. 2. The same as figure 1, but for case 2.

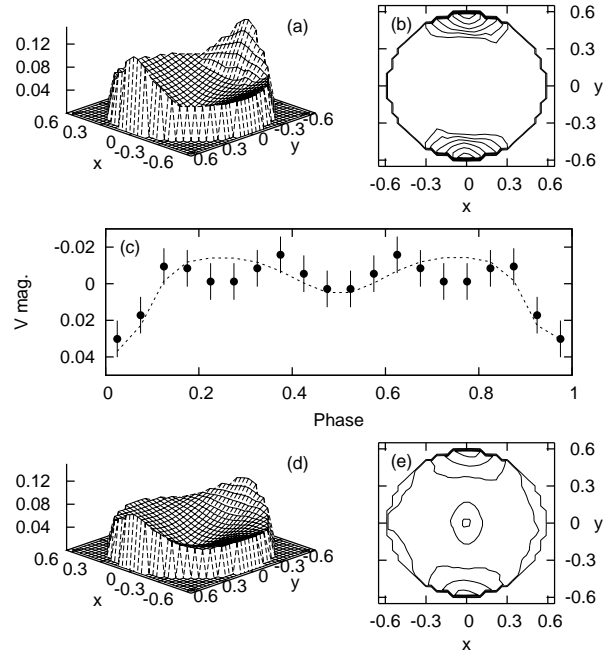


Fig. 3. The same as figure 1, but for case 3.

region. The peak height is 0.05 at $r = 0.14$ ($h/r = 0.37$). As can be seen from figures 1 and 2, the obtained height maps successfully reproduce the general profile of the assumed disk structures. It should be emphasized that the model can properly resolve the structures in the radial direction, namely in the outer (case 1) and inner (case 2) structures, as well as the azimuthal direction. In case 3, the disk has two flaring parts. Each of them has the same structure as case 1. This is actually expected in double-peaked early superhumps. The model again succeeded in reconstructing the two-flaring structure, as can be seen in figure 3.

On the other hand, those demonstrations indicate that the early superhump mapping could produce spurious signals in the estimated height map. First, the peak heights are underestimated in all cases. The peaks were assumed to be $h/r = 0.23$ and 0.37 in cases 1 and 2, although they were $h/r = 0.16$ and 0.23 in the reconstructed maps, respectively. In addition, the flaring areas were overestimated, or smeared out. These results were obtained because the prior distribution, π_{smooth} favors smooth structures. As a result, the model light curves partly failed to reproduce the substructures of the light curves; in figures 1 and 2, we can see dips around phase 0.25 in the light curves, which are not reproduced by the model. This dip is caused by occultation of the inner regions by the assumed flaring parts. In the reconstructed height map, this flaring part should be higher than the estimated one in order to reproduce the dips. However, a disk with such a spiky structure reduces π_{smooth} , and thereby reduces the posterior probability. Thus, our model could fail to reproduce highly localized, or quite steep height-structures in the disks. In principle, those smoothing effects could be less significant if we apply a high w in π_{smooth} . A high w , however, leads to a slow convergence and mixing in the MCMC procedure (for a detail, see the Appendix).

Second, in case 3, low h regions appear in both the left and right sides in the outermost parts in the reconstructed height map. The height was assumed to be constant at $h/r = 0.10$ in the outermost region, except for the flaring parts. The model estimated $h/r \sim 0.07$ in the left and right sides. As a result, the reconstructed disk apparently has not a circular, but a box-like height-map. This is also an artifact generated by π_{smooth} . We should discuss reconstructed height-maps while paying attention to this low h pattern when the double-peaked light curves are analyzed.

Finally, we can see that the height of the innermost region is slightly overestimated in all cases. They are estimated as $h/r \sim 0.12$. This is due to the prior distribution, π_{disk} . Since it is a product of truncated normal distributions, as defined in equation (5), its median is slightly larger than h_{disk} . In the artificial data, the light source is mainly in an outer region of the disk, and the contribution of the innermost region is relatively small. Hence, the height there almost follows π_{disk} , and thereby slightly large h are obtained.

Thus, we have demonstrated that our method can reconstruct the general trend of accretion-disk structures,

while reconstructed disks have several noteworthy artifacts in their structure. In the next section, we apply this model to real observations of early superhumps in V455 And. The parameter dependence is also discussed in the next section.

3. Results

3.1. Data and Model Parameters

We have applied our Bayesian model to the data of V455 And reported in Paper I. V455 And is a WZ Sge-type dwarf nova, whose first-ever-recorded superoutburst was discovered in 2007 September. Their observation revealed color variations associated with early superhumps for the first time (see section 1). Paper I reports simultaneous 6-band, g , V , R_c , I_c , J , and K_s -band data on JD 2454354, which is the fifth day (Day 5) since the outburst maximum. We used the blue five-band observations on Day 5 for the present study, since Paper I suggests that the K_s -band flux needs another emitting source in addition to the disk. High quality data not of all the five bands, but of two bands (V and J -band) were also available on JD 2454352 (Day 3). We can study the temporal evolution of the disk structure using those two sets of data.

The light curves were phase-averaged into 20 bins. Our model considers eclipses of the disk by the secondary star. Hence, the epoch of ephemeris is important for the conversion from time to phase, because the timing of eclipses is sensitive to the orbital phase. Araujo-Betancor et al. (2005) derived an ephemeris of V455 And using pre-outburst data between 2000 and 2003; $\text{HJD}2451812.67765(35) + 0.05630921(1) \times E$. Based on eclipse observations after the 2007 superoutburst (Kato et al. 2009), we found that the orbital phase of the mid-eclipses is shifted by $\Delta\phi = -0.01$ from those defined by the ephemeris in Araujo-Betancor et al. (2005). It is quite likely that the phase shift is simply due to accumulated errors in the ephemeris. In the present study, we calculated the orbital phase with the ephemeris presented by Araujo-Betancor et al. (2005), and then added $+0.01$ to the phase. The phase-averaged light curves on Day 3 and 5 are shown in figures 4 and 5, respectively.

We can see several characteristic features of early superhumps in figures 4 and 5. The light curves have a double-peaked profile; the secondary maxima are followed by the primary maxima. The amplitude of the hump decreases with time, from 0.3 mag on Day 3 to 0.2 mag on Day 5. A noteworthy feature in the Day 3 light curves is that the minima of early superhumps are slightly shifted from the orbital phase 0.0. This implies that the emitting source has a highly asymmetric structure. It is also noteworthy that the secondary minimum was quite deep on Day 5. It is even deeper than the primary minimum in the blue g and V -bands.

In the case of V455 And, intermittent short-term variations were occasionally superimposed on early superhumps (see Paper I). For example, we can see a sharp spike at phase 0.62 in the light curve on Day 5. The observed light curve on Day 5 is shown in figure 5 of Paper I.

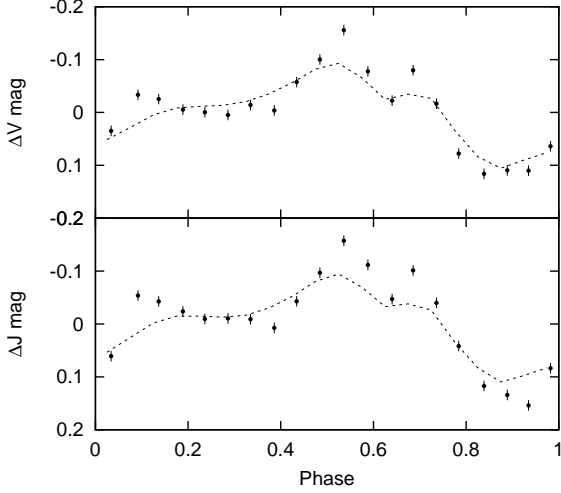


Fig. 4. Light curves of early superhumps of V455 And on Day 3. The upper and lower panels show V and J -band light curves, respectively. The filled circles represent the observed light curves. The small vertical bars indicate typical photometric errors of 0.01 mag. The dashed lines indicate the model light curves. The magnitudes are differential ones from the average magnitudes for each band.

As can be seen from that figure, a temporary sharp spike appeared just after a primary maxima not in all humps, but only in a hump. Another spike-like feature can be seen also in the light curve on Day 3 at phase 0.68. Their short time-scale implies that they were originated from an inner high-temperature region, and have a different mechanism (also see, Dmitrienko 2011). It is difficult to reproduce those spike-like features by our early superhump mapping, as mentioned in subsection 2.3. However, it is not a serious problem in the present study because we focus on stable and global structures of the disk.

The model contains several parameters to be determined. They are about the geometry of the binary and MCMC calculation. The binary-parameters include the inclination angle, i , the outer and inner radii, r_{out} and r_{in} , the inner (or outer) temperature, T_{in} (or T_{out}), and mass ratio, $q (\equiv M_2/M_1)$. Araujo-Betancor et al. (2005) reports that the inclination angle of V455 And is $i \sim 75$ deg based on the presence of shallow eclipses in its quiescent light curve. We used it in this study. We can estimate q using the empirical relationship between the superhump-period excess and q . According to Kato et al. (2009), the superhump period excess of V455 And is $\varepsilon = (P_{\text{SH}} - P_{\text{orb}})/P_{\text{orb}} = 0.015$, and the relation between ε and q is $\varepsilon = 0.16q + 0.25q^2$. Hence, the mass ratio of V455 And can be estimated as $q = 0.083$. Assuming a white dwarf having a mass of $M_{\text{WD}} = 0.6M_{\odot}$ (Araujo-Betancor et al. 2005) and a radius of $R_{\text{WD}} = 0.012R_{\odot}$ (Provencal et al. 1998), we can then calculate the binary separation to be $a = 3.7 \times 10^{10}$ cm. The model calculation was performed with $r_{\text{in}} = R_{\text{WD}}$ and $r_{\text{out}} = 0.6a$. This r_{out} condition is expected from the 2:1 resonance radius (Osaki, Meyer 2002).

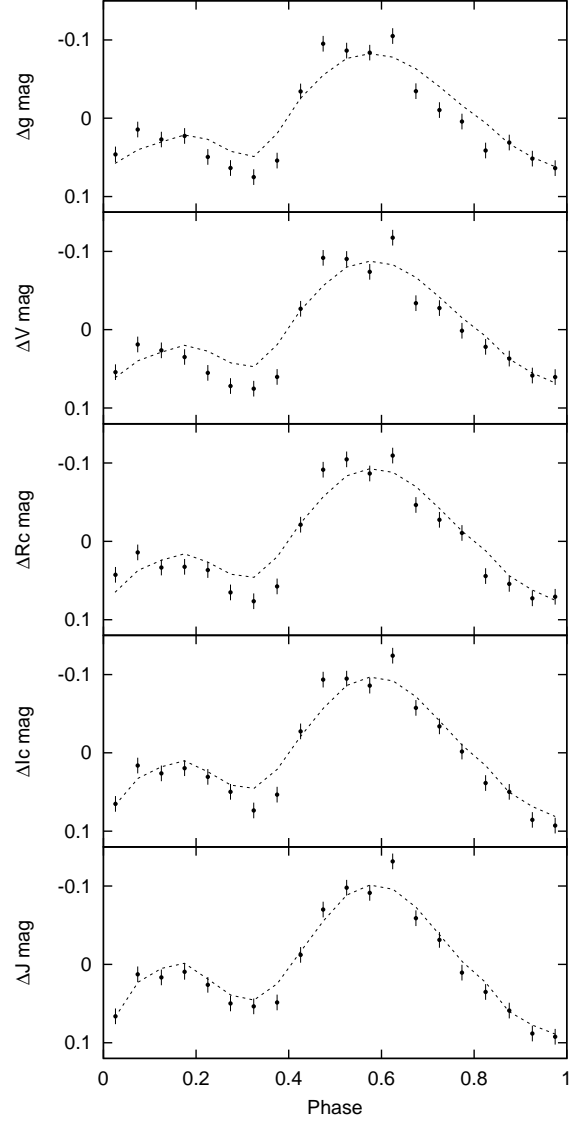


Fig. 5. Same as figure 4, but for Day 5. From top to bottom, the panels show g , V , R_c , I_c , and J -band light curves.

The innermost disk temperature, T_{in} , can be estimated from observed colors of V455 And. They were $g - V = 0.015$, $V - R_c = 0.052$, $R_c - I_c = 0.039$, and $I_c - J = -0.090$ on Day 5 (Paper I). These are compared with the model color of an axisymmetric disk with $h = h_{\text{disk}}$ and T_{in} . The best-fitted temperature is $T_{\text{in}} = 8.2 \times 10^4 \text{ K}$ (or $T_{\text{out}} = 6.9 \times 10^3 \text{ K}$) for the Day 5 data. In the same manner, the $V - J$ color of -0.034 on Day 3 yields $T_{\text{in}} = 8.6 \times 10^4 \text{ K}$ (or $T_{\text{out}} = 7.3 \times 10^3 \text{ K}$).

We summarize the model parameters for the analysis of the V455 And data in table 1. In the next subsection, we report on the reconstructed height maps calculated with those parameters for the Day 5 data. In subsection 3.3, we discuss the parameter dependence of the result by comparing the reconstructed height maps obtained with different sets of T , r_{out} , i , and q .

3.2. Early Superhump Mapping for the Day 5 Data of V455 And

We estimated $\{h(r, \theta)\}$ using the data on Day 5 of V455 And with the model parameters discussed in the last subsection. The estimated $\{h(r, \theta)\}$ are represented by the height maps shown in figure 6. The upper and lower panels show the height maps of $h(= h/a)$ and h/r , respectively. The model light-curves calculated with this $\{h(r, \theta)\}$ are indicated by the dashed lines in figure 5. We can see that the observed light-curves are well reproduced by the model. It apparently fails to reproduce short-term variations, such as a spike-like feature at phase 0.62. This can be explained by the fact that π_{smooth} favors smooth structures, as mentioned in section 2 and also in the last subsection. The secondary minima of the model light curves are slightly shallower than the observed ones, particularly in the blue bands.

The maximum h region is distributed in the outermost part of the right-lower quadrant of the map, as shown in figure 6. This part is responsible for the primary maximum in the light curve. The highest point in the disk is $h_{\text{max}} = 0.12$ at an outermost point of $(x, y) = (+0.36, -0.48)$ ($h/r = 0.20$). The elevation angle of this point from the disk center is, $\arctan(h_{\text{max}}/r_{\text{out}}) = \arctan(0.12/0.60) = 11 \text{ deg}$. This means that the center of the disk is occulted by this outermost flaring part in the case of $i \gtrsim 79 \text{ deg}$. The secondary maximum in the light curve is generated by a flaring outermost part in the left-upper quadrant of the map. The maximum h in this part is $h = 0.09$ at $(-0.49, +0.34)$ ($h/r = 0.15$). This is smaller than h_{max} . Hence, the difference between the amplitudes of the primary and secondary maxima can be explained by the difference between the heights of the corresponding flaring parts.

In addition to those two major features, we can see flaring arm-like patterns elongated to relatively inner parts of the disk. They can be seen more conspicuously in the lower panel of figure 6. In the left-lower quadrant, there is a “spot”-like high region, which could be connected to the primary maximum part in the right-lower quadrant. This region includes the largest h/r point among the whole disk, $h/r = 0.26$ at $(-0.16, -0.21)$. The observed deep

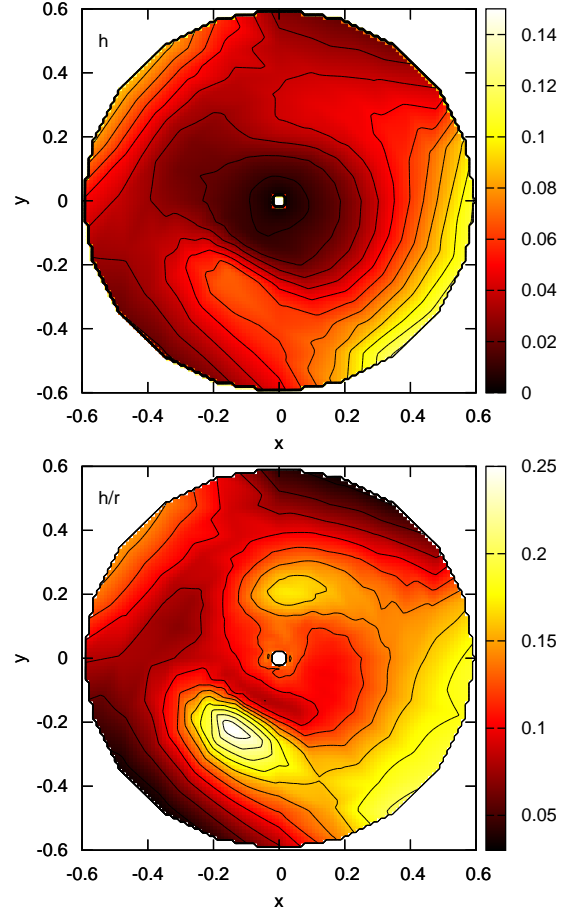


Fig. 6. Height map for the data on Day 5 of V455 And. The upper and lower panels show maps of $h(= h/a)$ and h/r , respectively. Both the contours and color-maps represent the same maps. The upper panel shows contours of $h = 0.00$ – 0.15 with an interval of 0.01 . The lower panel shows contours of $h/r = 0.00$ – 0.25 with an interval of 0.02 . The secondary star is located at $(x, y) = (1.0, 0.0)$.

secondary minimum in the light curves is generated by the occultation of inner regions by this flaring area. The relatively shallow secondary minimum of the model light curves implies that the flaring part would originally have a more localized structure with larger h than the reconstructed disk. The other arm-like pattern can also be seen in the right-upper quadrant. Its h/r are relatively moderate ($h/r \sim 0.19$) compared with those of the left-lower arm.

There are low regions in the outermost parts of both the left-lower and right-upper quadrants. This could be partly due to the spurious signal, as mentioned in subsection 2.3. However, the height in those regions is even smaller than that of case 3 in subsection 2.3 in which $h/r \sim 0.07$; in the case of figure 6, the minimum h point at $(-0.34, -0.49)$ has $h/r = 0.03$. It indicates that those low regions are not only a totally spurious signal, but also an intrinsic feature of the disk.

Table 1. Model parameters

Case	r_{out}/a	r_{in}/a	$T_{\text{in}} (\times 10^4 \text{ K})$	$T_{\text{out}} (\times 10^3 \text{ K})$	$i \text{ (deg)}$	q
1,2,3 (subsection 2.3)	0.60	0.020	8.7	7.3	75.0	0.11
Day 5 (default)	0.60	0.022	8.2	6.9	75.0	0.083
Day 3 (default)	0.60	0.022	8.6	7.3	75.0	0.083
A	0.60	0.022	8.0	6.8	70.0	0.083
B	0.60	0.022	8.7	7.3	80.0	0.083
C	0.60	0.020	8.9	7.5	75.0	0.11
D	0.60	0.022	8.2	6.9	75.0	0.067
E	0.60	0.022	7.2	6.1	75.0	0.083
F	0.60	0.022	9.2	7.8	75.0	0.083
G	0.70	0.022	9.2	6.9	75.0	0.083
H	0.50	0.022	7.3	7.0	75.0	0.083
Day 5 (irradiated, $T_{\text{cs}} = 1.2 \times 10^5 \text{ K}$)	0.60	0.022	6.0	5.8(min), 13.4(max)	75.0	0.083
Day 5 (irradiated, $T_{\text{cs}} = 2.0 \times 10^5 \text{ K}$)	0.60	0.022	6.0	5.8(min), 22.1(max)	75.0	0.083

3.3. Dependence on the Model Parameters

In this subsection, we examine the dependence of the result reported in the last subsection on the assumed parameters. We recalculated the height maps for eight sets of different parameters of i , q , T_{in} , and r_{out} listed in table 1, as labeled from cases A to H. Their height maps and model light-curves are depicted in figure 7 and 8, respectively. In both figures, the middle-column panels show the same maps and light-curves as reported in the last subsection.

The dependence of the result on i can be seen in cases A and B, in which we set $i = 70.0$ and 80.0 deg, respectively. These changes in i required us to readjust T_{in} to be consistent with the observed colors. We calculated $T_{\text{in}} = 8.0 \times 10^4 \text{ K}$ for case A and $8.7 \times 10^4 \text{ K}$ for case B. The other parameters are the same as those of the default ones. As can be seen in figure 7, the global pattern of the height map is apparently insensitive to i , while there are minor differences in the maps with different i . First, the disk height apparently decreases as the increase in i . This can be explained as follows: the amplitude of the humps can be considered as a ratio of the projected area of high h region to low h region on the plane perpendicular to the viewing direction. With a given height map, the area ratio decreases with a decrease in i . Second, the model light curve of case A fails to reproduce the deep secondary minimum, as can be seen in figure 8. In a smaller i case, like case A, the disk is required to have higher h to explain the observed amplitude. However, quite high h values reduce the posterior probability, because π_{disk} becomes small. Hence, the reconstructed map with a small i fails to reproduce substructures in the light curve.

Another noteworthy feature of the height map is a high region around $(x, y) = (0.6, 0.0)$, which is unnaturally confined to a small region. It is most prominent in case A, and less prominent in higher i cases. This high region means that the inner region of the disk is required to be occulted at phase ~ 0.0 to explain the observation. In a high- i case (case B), the eclipse by the secondary star plays a role in hiding the inner region, and thereby the

high region around $(x, y) = (0.6, 0.0)$ disappears. It implies $i \gtrsim 75$ deg for V455 And in order to avoid making this unnatural feature.

The mass ratio, q , is one of the most uncertain parameters, while the reconstructed height maps are insensitive to small changes in q , as shown in cases C and D in figure 7 and 8. The height maps and light curves of cases C and D were calculated with $q = 0.11$ and 0.067 , respectively. In case C, a large q slightly changes the binary separation, the inner radius, and as a result, the inner temperature, as shown in table 1. The changes in those parameters are negligible in case D. The mass-ratio of case C corresponds to $\varepsilon = 0.021$, which is the largest ε among WZ Sge stars having very short P_{orb} of $< 0.057 \text{ d}$ (Kato et al. 2009). The mass-ratio only has a minor effect on the results, because it is only related to the eclipse by the secondary star. The mass-ratio is so small, even in case C, that the small changes in q only lead to small changes in the Roche lobe geometry. Hence, the uncertainty in q has no significant effect on the results in the case of WZ Sge stars.

The innermost temperature, T_{in} , was estimated from the observed color. While we use $T_{\text{in}} = 8.2 \times 10^4 \text{ K}$ in the last subsection, it has a $1\text{-}\sigma$ error of $0.4 \times 10^4 \text{ K}$. Hence, we should check the dependency of the result on T_{in} . In cases E and F, we estimate $\{h\}$ with $T_{\text{in}} = 7.2$ and $9.2 \times 10^4 \text{ K}$, which correspond to $T_{\text{out}} = 6.1 \times 10^3$ and $7.8 \times 10^3 \text{ K}$, respectively. The reconstructed height-maps are consistent each other, as can be seen from figure 7. Thus, the reasonable changes in temperature have no significant effect on the results of the early superhump mapping.

Next, we evaluate the dependency of the results on the outer disk-radius, r_{out} . We used $r_{\text{out}}/a = 0.6$ in the last subsection, which is expected from the 2:1 resonance radius (Osaki, Meyer 2002). It has, however, not been confirmed by observations. In cases G and H, the height maps were calculated with $r_{\text{out}}/a = 0.7$ and 0.5 , respectively. According to Osaki, Meyer (2002), the disk radius of case G is close to the 3:1 resonance radius in WZ Sge stars. The disk radius of case H corresponds to the maximum radius allowed by the tidal truncation. It is note-

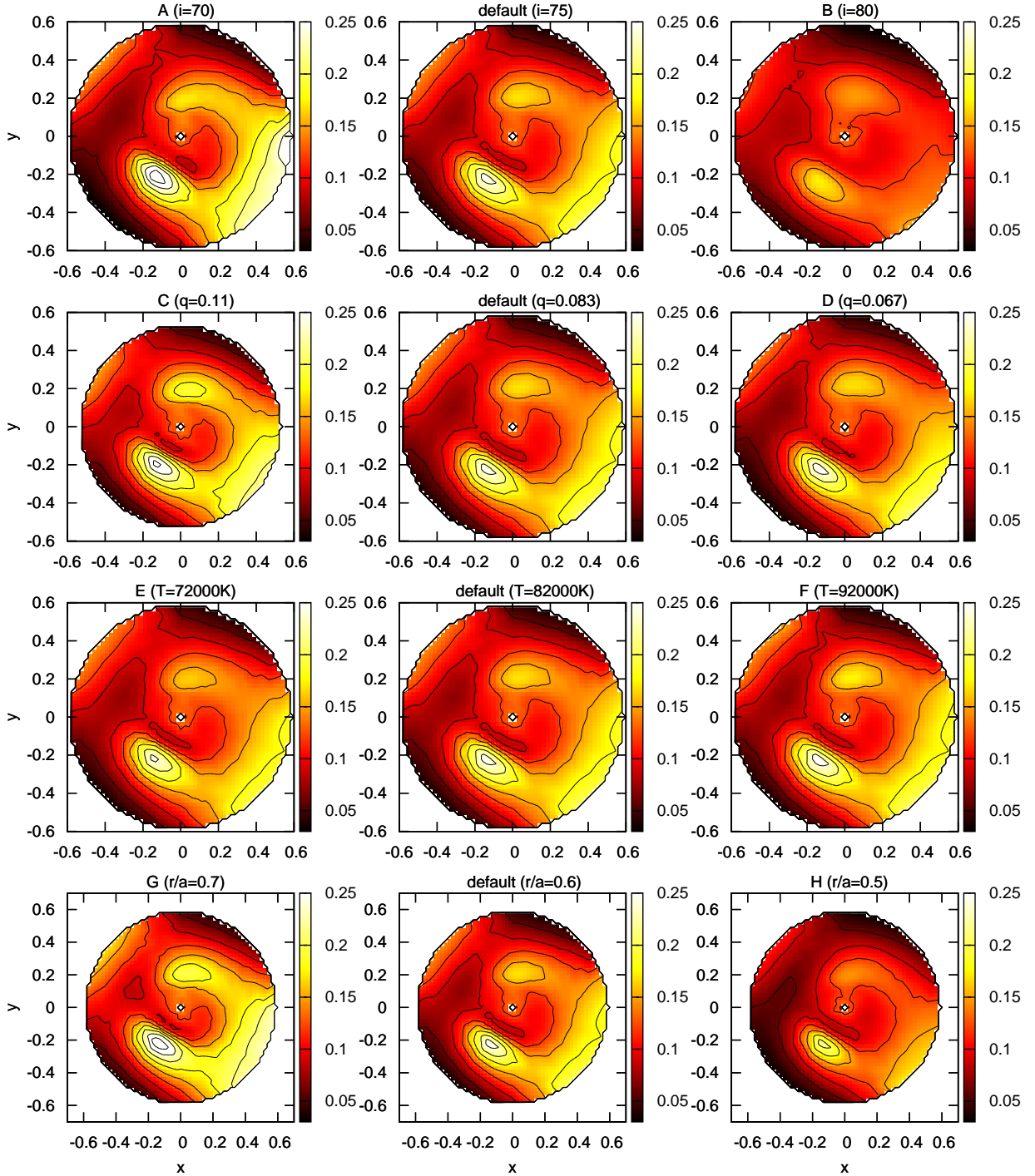


Fig. 7. Height maps calculated from the data on Day 5 of V455 And for different parameters. The contours are shown from $h/r = 0.00$ – 0.27 with an interval of 0.03 . The secondary star is located at $(x, y) = (1.0, 0.0)$. The model parameters for each case are listed in table 1. From top to bottom, they were calculated with different i , q , T_{in} , and r_{out} , respectively. All middle-column panels are the same as figure 6, shown for a comparison.

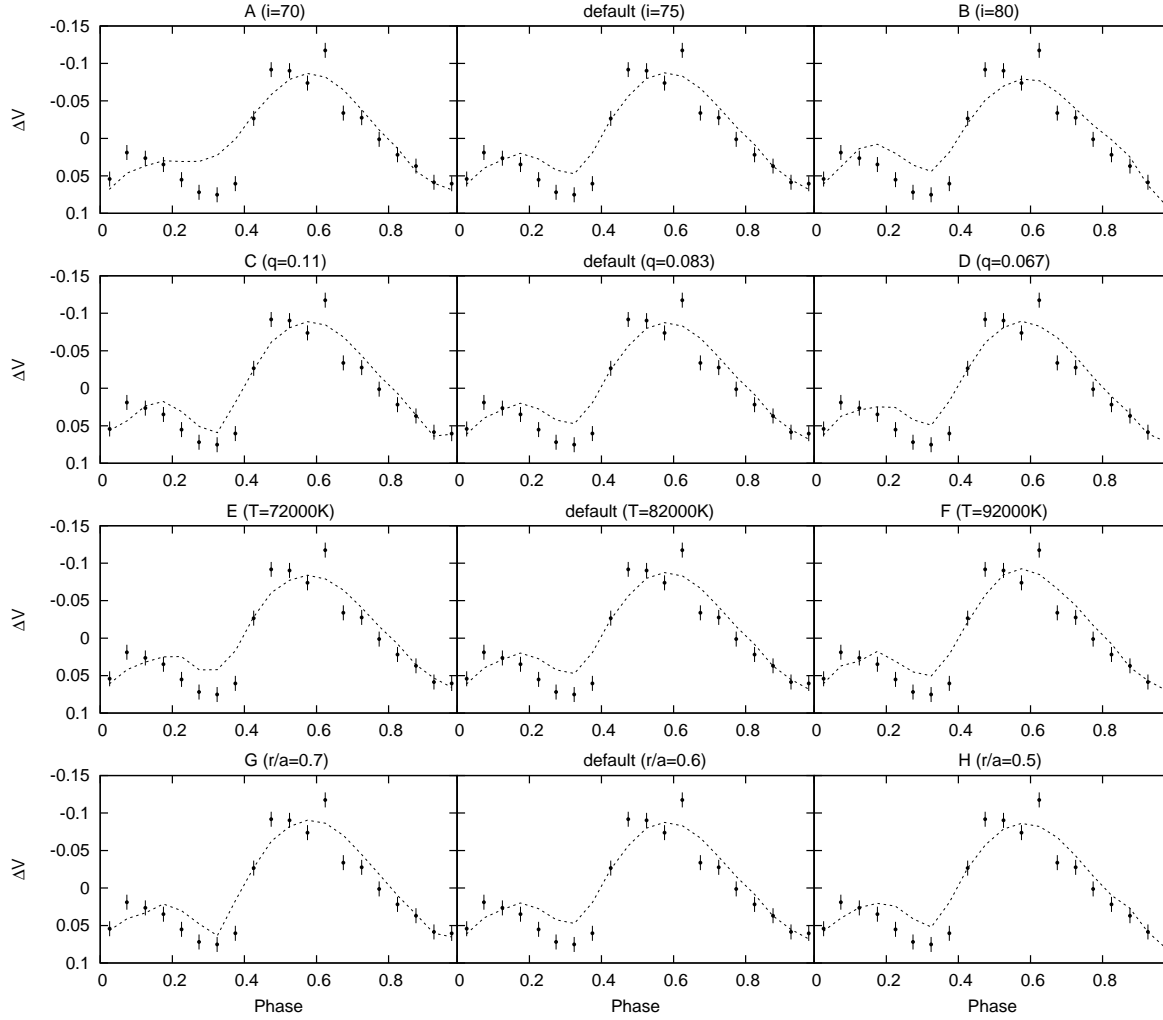


Fig. 8. Model light curves calculated from the data on Day 5 of V455 And for different parameters, indicated by the dashed lines. The filled circles indicate the observed light curves. The model parameters for each case are summarized in table 1. From top to bottom, they were calculated with different parameters i , q , T_{in} , and r_{out} . All middle-column panels are the same as figure 5, shown for comparison.

worthy that the h/r maps are quite similar in all cases with $r_{\text{out}}/a = 0.5$, 0.6 , and 0.7 . As a result, h is larger in the case with larger r_{out} .

Thus, the results of the early superhump mapping are insensitive to reasonable changes in the model parameters, i , q , T_{in} , and r_{out} . The inclination angle has a relatively large effect on the result.

Finally, we discuss the dependence of the reconstructed height map on the number of data. We evaluate it by comparing the height map calculated with two-band data with that with five-band data. Figure 9 shows the light curve (upper panel) and height map (lower panel), which were calculated from V - and J -band data of V455 And on Day 5, instead of all five-band data. Compared with figures 5 and 6, the result obtained with the two-band data reproduces the major features of the height map obtained with the five-band data: the two outermost flaring regions and two inner arm-like patterns. The maximum h in the

height map calculated from the two-band data is only 6% smaller than that from the five-band data. The structures in both the light curve and height map are smoother than those obtained from the five-band data. This is due to the small amount of data, which makes the weight of the likelihood function small with respect to the prior probability.

Thus, we can obtain reconstructed height maps with a reasonable degree of accuracy, even in the case that only two-band data is available. High quality data were obtained on Day 3 in Paper I, but only in the V and J -bands. In the next subsection, we report the results obtained from the data on Day 3.

3.4. Early Superhump Mapping for the Day 3 Data of V455 And

We estimated $\{h(r, \theta)\}$ using the V and J -band data on Day 3 of V455 And. The model parameters are listed

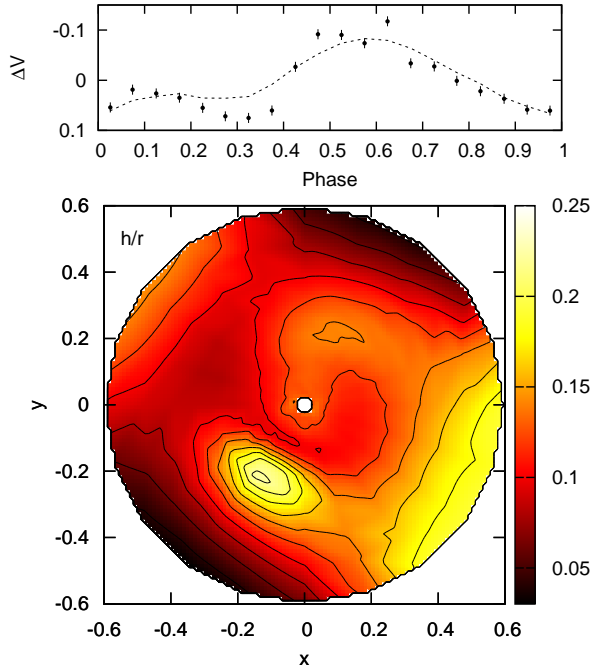


Fig. 9. Light curve (upper) and height map (lower) calculated from the V and J -band light curves on Day 5 of V455 And. In the upper panel, the filled circles represent the observed light curves. The dashed line indicates the model light curve. The color maps and contours represent h/r . The contours are shown from $h/r = 0.00$ – 0.25 with an interval of 0.02 , the same as figure 6. The secondary star is located at $(x, y) = (1.0, 0.0)$.

in table 1. The reconstructed height map on Day 3 is shown in figure 10. The model light-curve is indicated by the dashed line in figure 4. The height map on Day 3 has common features with that on Day 5: the outermost flaring parts for the primary and secondary maxima of the light curve and the inner arm-like patterns.

On the other hand, there are several differences in the detailed structures between them, which represent a temporal evolution of the disk. The maximum height in the outermost part is $h/r \sim 0.25$ on Day 3, while it is $h/r \sim 0.20$ on Day 5. The amplitude of the light curve on Day 3 is larger than that on Day 5. The large amplitude on Day 3 is, therefore, due to the large h . We confirmed that the disk temperature has only minor effect on the amplitude; the amplitude keeps small with ~ 0.2 mag in the light curve calculated with the height map on Day 5 and the temperature on Day 3. In general, early superhumps decrease in amplitude with time. Our result suggests that it is due to the decrease in the disk height in the outermost region, rather than a decrease of the disk temperature.

Another noteworthy feature is the arm patterns. In figure 10, the right-upper arm has the largest h/r on Day 3, while the left-lower arm has the largest h/r on Day 5. The weakening of the left-lower arm is due to the shallow secondary minimum in the light curve on Day 3. No highly flaring region is required to reproduce such a shal-

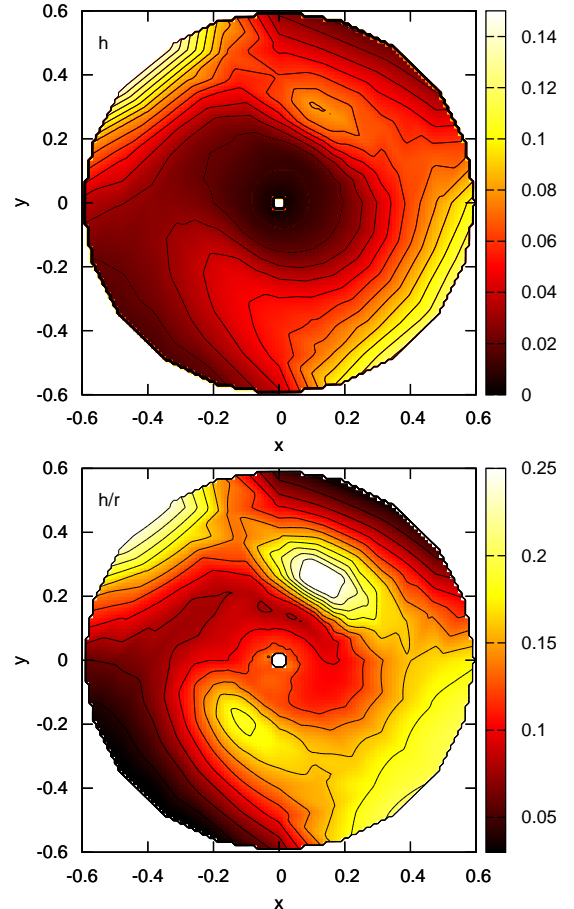


Fig. 10. Same as figure 6, but for Day 3.

low secondary minimum. The strong right-upper arm is required to reproduce the small dip at phase ~ 0.63 in the light curve. This dip feature may, however, be related to the short flare-like feature around phase ~ 0.68 ; the small dip feature could be a spurious signal generated by the intermittent short flare. The height of the right-upper arm could be overestimated if the flare-like feature around phase ~ 0.68 has a different origin from early superhumps.

4. Discussion

4.1. Implication from the Reconstructed Disks

Here, we compare the reconstructed disk-structures with theoretical ones which have been proposed for the origin of early superhumps. As mentioned in section 1, Kato (2002) propose the tidal distortion scenario, while Osaki, Meyer (2002) propose the 2:1 resonance scenario.

Ogilvie (2002) calculate the disk structure which is tidally distorted. They present the height map of a disk in a binary system with $q = 0.5$ in their figure 2. The tidally distorted disk also has two flaring parts in its outermost region. We find that the phases of the outermost flaring parts are consistent with those of our reconstructed map. In addition, the inner arm-pattern shown in their figure is

reminiscent of the arm-pattern in the right-upper quadrant of the reconstructed image in figure 6. Thus, the global structure of the reconstructed image is similar to that expected from the tidal distortion.

However, the tidal distortion scenario cannot explain the arm-like pattern in the left-lower quadrant of the reconstructed image. This pattern is responsible for the secondary minimum in the light curve. As mentioned in subsection 3.2, that area has a quite large h/r , and possibly has a spot-like structure, rather than arm-like one. In conjunction with the height map on Day 3, this feature probably evolved from Day 3 to 5. Two scenarios can be considered to explain this flaring area. First, an additional effect may be responsible for it. The tidal effect may affect the global structure of the disk, while it is difficult to make such a well-localized structure. It could be related to the accretion stream from the secondary star or the evolving ordinary superhump. However, these scenarios are highly speculative. Second, it is possible that the inner arm-like pattern is a spurious structure if the model assumptions are not valid for the real structure of the disks. In this case, the most controversial assumption is the temperature distribution of the disk, namely $T = T_{\text{in}}(r/r_{\text{in}})^{-3/4}$. If the temperature distribution is not axisymmetric, it could make a height map without the inner flaring region. The irradiation effect may be able to achieve such a condition. We evaluate it in the next subsection.

We should note that the height distortion calculated by Ogilvie (2002) is for a binary system of $q = 0.5$, which is much larger than those of WZ Sge stars ($q \lesssim 0.1$). Detailed studies should be carried out with theoretical disk-structure calculated with appropriate mass-ratios in the future. Kunze (2004) present SPH simulations of disks which extend to the 2:1 resonance radius (also see, Kunze, Speith 2005). Their result shows a two-armed density wave close to the outermost region in the disk. The phases of this two-armed pattern are consistent with the outermost flaring regions of our reconstructed map. However, it is difficult to compare the result of their SPH simulation directly with our height map. A study of the height distortion expected from the SPH simulations is also required in future.

4.2. Effect of Irradiation

We evaluate the effect of irradiation to the early superhump mapping in this subsection. The temperature in the outermost flaring parts would increase by the irradiation effect. If this is the case, the temperature distribution could be non-axisymmetric, which may change the structure of the reconstructed height maps. The irradiation effect depends on the luminosity and geometry of the source for irradiation and the albedo of the irradiated surface. Unfortunately, those parameters are poorly known. In outbursting dwarf novae, the most powerful source for irradiation is supposed to be boundary layers, which are formed between the WD surface and the disk. X-ray and UV observations suggest that its temperature is typically on the order of 10^5 K, while its size is poorly known (e.g.,

Long et al. 1996; van der Woerd 1987; Mauche, Raymond 2000). The temperature and geometry of boundary layers definitely depend on the accretion rate, which can change during outbursts. However, no estimation of the temperature and size of the boundary layer has been reported for V455 And. Furthermore, V455 And is known as an intermediate polar (Araujo-Betancor et al. 2005). Its physical condition in the innermost region of the disk could be different from that of non-magnetic dwarf novae in outburst. Here, we focus on how the irradiation effect changes the disk structures estimated by the early superhump mapping. Hence, we consider an extreme condition that the total luminosity, L_{tot} , is dominated not by the luminosity generated by the viscous heating, L_{vis} , but by the irradiation luminosity, L_{irr} , in the outermost part.

We calculated the irradiation effect using a similar method reported in Hachisu, Kato (2001); a patch on the disk surface is irradiated by the central source and other patches if there is no blocking patch between the centers of the source and patch. The central source for irradiation, which is probably dominated by the boundary layer emission, has a luminosity of $L_{\text{cs}} = 4\pi r_{\text{in}}^2 \sigma T_{\text{cs}}^4$. We assume that the radiation from the central source is isotropic. Consider a patch, $p_i = p(r, \theta)$, whose size and normal vector are s_i and \mathbf{n}_i . The patch p_i receives energy from the central source by irradiation, and releases the energy by radiation with a luminosity $L_{\text{irr},\text{cs}}$, which is calculated as

$$L_{\text{irr},\text{cs}} = \eta \xi_{ci} \frac{L_{\text{cs}}}{4\pi r^2} s_i (\mathbf{n}_i \cdot \hat{\mathbf{r}}_{ic}), \quad (6)$$

where η is the fraction of the absorbed energy to the total irradiated energy in p_i . ξ_{ci} is 1 if there is no blocking patch between the centers of the source (the disk center in this case) and the patch. Otherwise, $\xi_{ci} = 0$. $\hat{\mathbf{r}}_{ic}$ denotes the unit vector in the direction of the patch center from the disk center. Using a similar notation, the irradiation luminosity by other patches is

$$L_{\text{irr},\text{disk}} = \eta \sum_{j \neq i} \xi_{ij} \frac{\sigma T_j^4}{2\pi r_{ij}^2} s_j (\mathbf{n}_j \cdot \hat{\mathbf{r}}_{ji}) s_i (\mathbf{n}_i \cdot \hat{\mathbf{r}}_{ij}). \quad (7)$$

The total luminosity of p_i is, hence,

$$\sigma T_{\text{irr}}^4 s_i = L_{\text{tot}} = L_{\text{vis}} + L_{\text{irr},\text{cs}} + L_{\text{irr},\text{disk}}. \quad (8)$$

The original luminosity, L_{vis} , is calculated as $L_{\text{vis}} = \sigma T_{\text{org}}^4 s_i$, where T_{org} is a temperature given by an assumed temperature distribution. The temperature of the irradiated patch, T_{irr} , is given by equation (8).

The structure of irradiated disks was estimated by iteratively using our method of the early superhump mapping described in section 2. In the n -th iteration, we calculate a height map, $\{h\}_n$ with an old temperature distribution. Then, a new temperature distribution is defined by $\{T_{\text{irr}}\}_{n+1}$ which is given by the calculation described above. We calculate a new height map, $\{h\}_{n+1}$ using the new temperature distribution. This process is repeated until $\{h\}_n$ converge. The analysis of the data of V455 And requires 4–5 iterations for convergence. The initial temperature distribution is given by a standard one, that is,

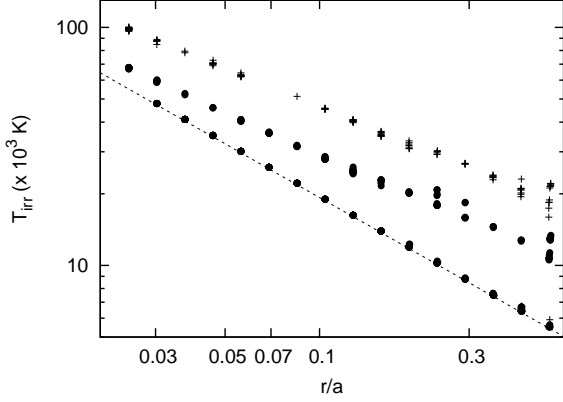


Fig. 12. Radial distribution of temperature of the irradiated disk. The filled circles and crosses denote those with $T_{\text{cs}} = 1.2$ and 2.0×10^5 K, respectively. The dashed line indicates the standard temperature distribution, that is, $T = 6.0 \times 10^4 (r/r_{\text{min}})^{-3/4}$.

$T = T_{\text{in}}(r/r_{\text{in}})^{-3/4}$, while we confirmed that the final result is insensitive to the initial distribution.

We calculated the irradiated disk structure using the data on Day 5. The resultant height maps are shown in figure 11. The left panels are obtained with $\eta = 0.5$ and $T_{\text{cs}} = 1.2 \times 10^5$ K, and $T_{\text{in}} = 6.0 \times 10^4$ K. The colors of the reconstructed disk are consistent with the observation within a color index of 0.03. The other model parameters are listed in table 1. Figure 12 shows the radial distribution of temperature of the irradiated disk, as indicated by the filled circles. We can see two sequences in the temperature; the high-temperature sequence corresponds to the patches irradiated by the central source. The low-temperature sequence corresponds to the non-irradiated patches in which the emission from the central source is blocked by other patches. A part of the outermost region is heated up to 1.3×10^4 K by the irradiation.

The most noteworthy feature of the irradiated disk is that the inner arm-like patterns are weaker than those estimated from the model without the irradiation effect. The arm-like pattern has the maximum h/r of 0.16 in the irradiated disks, although they have $h/r \sim 0.26$ in non-irradiated disks. The weakening of the arm-like pattern is due to an increase of the temperature of the outermost flaring regions. As mentioned in subsection 3.2, the inner arm-like pattern in the left-lower quadrant is responsible for the deep secondary minimum in the light curve on Day 5. This structure is required to occult the blue light originated from the inner high-temperature region. However, in the irradiated disks, the outermost flaring regions significantly contribute to the blue light. The deep secondary minimum can be reproduced if that phase corresponds to the position at which the contribution from those outermost high temperature regions is small.

On the other hand, the arm-like pattern can be seen even in the irradiated disk with $T_{\text{cs}} = 1.2 \times 10^5$ K, while it weakens. This supports the presence of this feature in the disk. The arm-like pattern almost disappears when

we assume a higher T_{cs} of 2.0×10^5 K. The right panels in figure 11 show height maps obtained with this high T_{cs} . However, the temperature of the outermost region can be quite high, 2.2×10^4 K, and the color of the reconstructed disk becomes so blue that it is inconsistent with the observation.

In addition to the irradiated disk, we evaluate the contribution from the irradiated secondary star. The contribution is expected to be low because the irradiated area by the central source is small; low-latitude regions are blocked by the disk. We calculated the irradiation effect of the secondary using the same manner as described above for the disk. The surface of the secondary was divided into 128 patches (16 and 8 bins in the longitude and latitude directions, respectively). The temperature was initially set to be 3000 K for all patches, and calculated with the irradiation effect for each patch. The model parameters for the disk was the same as the above case of $T_{\text{cs}} = 1.2 \times 10^5$ K (see table 1). As a result, we confirmed that the irradiated region is limited in a latitude of 35–80 deg. The maximum temperature is 1.3×10^4 K. The total flux from the irradiated secondary is < 0.02 times that from the irradiated disk. Its contribution is highest at phase 0.5, where the irradiated region is facing to us, and lowest at phase 0.0. This small contribution means that the amplitude of the light curve, which is caused by the geometrical effect of the disk, is 0.02 mag smaller than the observed light curve. Compared with the typical photometric error of 0.01 mag, it leads to a marginal difference in the disk structure. We subtracted the secondary-star contribution from the observed light curve, and re-calculated the disk structure. The resultant height map has a global structure the same as that without the secondary-star contribution, while the disk height at the outermost region is slightly smaller. Thus, the irradiated secondary star has no significant effect on the global structure of the reconstructed height map.

4.3. Structure of the Light Curves of Early Superhumps

Our analysis suggests that the eclipse by the secondary star plays a crucial role in determining the structure of the light curve around the primary minimum. Figure 13 shows the g - and J -band light curves on Day 3 and 5 with (the solid lines) and without (the dotted lines) eclipses. As can be seen in these light curves, the eclipses change the phases of the primary minimum and secondary maximum. It is most prominent in the J -band light curve on Day 5; the phase of the primary minimum is 0.875 if the eclipse is not taken into account, while it is about 0.000 in the eclipsed light curve. The phases of the secondary maxima are 0.075 and 0.175 in the light curves without and with eclipses, respectively. The phase shift of the primary minimum indicates that the phase of the flux minimum can be inconsistent with the orbital phase 0. In fact, the flux minimum preceded the orbital phase 0 in all of the light curves on Day 3, as can be seen in figure 13. Hence, the flux minimum cannot be used for determining the ephemeris of binaries, even in the case of an eclipsing system.

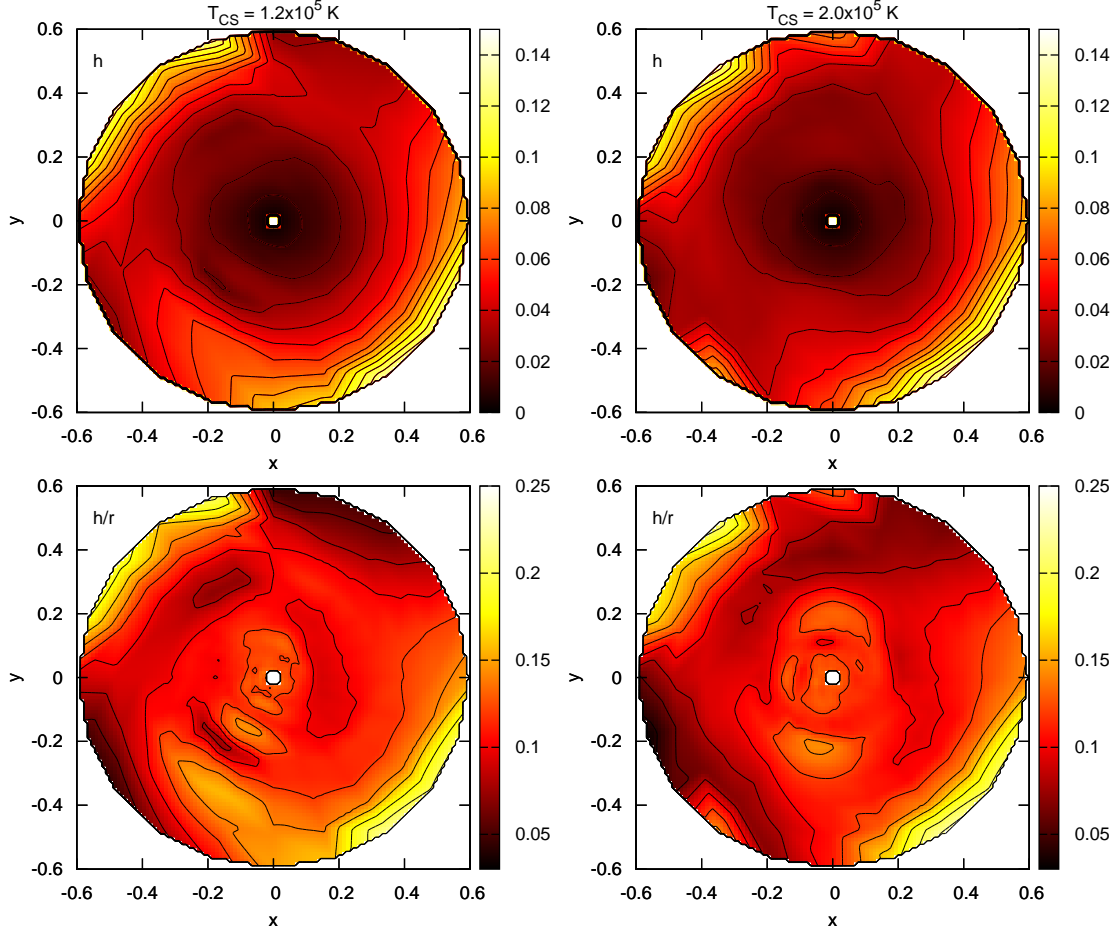


Fig. 11. Height maps of the irradiated disks calculated from the data on Day 5 with $T_{\text{CS}} = 1.2 \times 10^5$ K (left) and 2.0×10^5 K (right). The upper and lower panels show the maps of h and h/r , respectively. Both of the contours and color-maps represent the same h or h/r . The upper panel shows contours of $h = 0.00$ – 0.16 with an interval of 0.01 . The lower panel shows contours of $h/h_{\text{disk}} = 0.00$ – 0.26 with an interval of 0.02 . The secondary star is located at $(x, y) = (1.0, 0.0)$.

The results of our early superhump mapping can be used to predict the amplitude of the light curve depending on the inclination angle, i . Figure 14 shows the V -band model light-curves of early superhumps in different i , which were calculated by using the height map on Day 5. We can see a general trend that the light curves with higher- i have larger amplitudes. Figure 14 includes light curves up to $i = 80$ deg. In the case of $i > 80$ deg, the amplitude rapidly increases because of the eclipse of the inner region. It is over 1 mag when $i > 84$ deg. The amplitude of early superhumps is below 0.10 and 0.01 mag in $i < 60$ and < 20 deg, respectively. Kato et al. (2009) report several light curves of early superhumps, in which a lower limit of the amplitude is apparently ~ 0.02 mag. This can be considered as a detection limit of early superhumps with typical equipment that they used. The model light curve has an amplitude smaller than 0.02 mag in the case of $i \lesssim 30$ deg. If the direction of the rotation axis of binaries has a uniform distribution on the sphere, the probability distribution of systems having i is proportional to $\sin i$. Then, the fraction of systems having

$i > 30$ deg to all systems is calculated to be 0.87. This implies that early superhumps can be detected in most WZ Sge stars. Early superhumps were detected in 22 systems among 34 WZ Sge stars which are included in Kato et al. (2009). The fraction is 0.65, which is smaller than the expected one. This is probably because early stages of superoutbursts are occasionally overlooked. Our result implies that the fraction of the detection of early superhumps would increase if early stages are observed more frequently by prompt reports of outburst discoveries and follow-up time-series observations. We note that the above discussion is based on the data on Day 5, on which the amplitude of the early superhump was smaller than that on Day 3. The estimated amplitudes and fraction of the detection would be higher than the above values at the maximum of superoutbursts.

5. Summary

We have developed a method by which we can reconstruct the height map of accretion disks in dwarf novae using multi-band light curves of early superhumps. Using

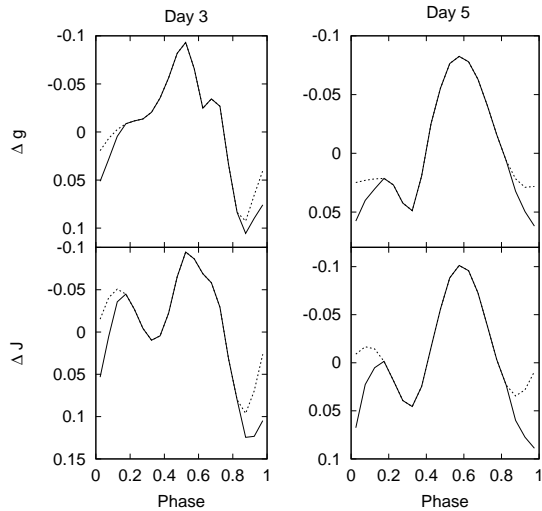


Fig. 13. Model light curves with and without eclipses. The left and right panels show those on Day 3 and 5, respectively. The upper and lower panels show their light curves in the g and J -bands, respectively. The eclipsed light curves (solid lines) are normalized by the average magnitudes in each band. The non-eclipsed light curves (dotted lines) are shifted to be consistent with the non-eclipsed light curves out of eclipses.

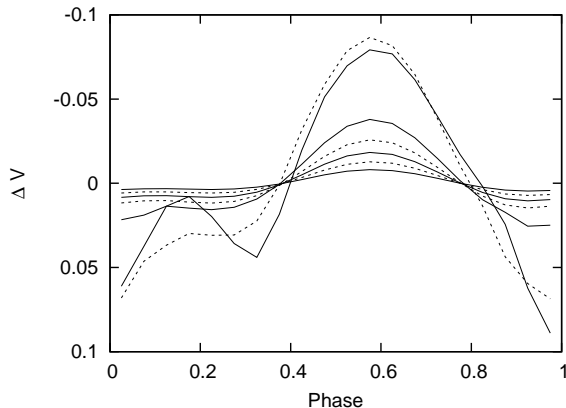


Fig. 14. Model light curves calculated from the height map on Day 5 for different i . From those having the smallest amplitude, the solid lines indicate $i = 20, 40, 60$, and 80 , and the dashed lines indicate $i = 30, 50$, and 70 .

this “early superhump mapping” method, we analyzed light curves of V455 And during its superoutburst. Our findings are summarized below.

- The reconstructed disk has a structure that has two flaring parts in the outermost region and two flaring arm-like patterns elongated to relatively inner parts of the disk.
- The maximum h/r reaches 0.25 and 0.20 on Day 3 and 5, respectively. We suggest that the decrease in the amplitude of early superhumps is mainly due to the decrease in the disk height in the outermost region.
- The overall pattern of the disk is reminiscent of the structure of tidally deformed disks. However, one of the inner arm-like patterns is difficult to be reproduced by the tidal deformation. That pattern is required by the deep secondary minimum in the observed light curves.
- It suggests that, in addition to the tidal effect, the disk is deformed by another unknown mechanism. Alternatively, our model may be failing to reproduce the characteristics of the disk in dwarf novae. We have confirmed that the disk structure with weaker arm-like patterns is optimal in the model including the irradiation effect. The strongly irradiated disk, however, gives quite blue colors which may conflict the observation.
- Our result predicts that early superhumps are detected in 87 % of WZ Sge stars with amplitudes of > 0.02 mag.

This work was partly supported by a Grand-in-Aid from the Ministry of Education, Culture, Sports, Science, and Technology of Japan (19740104, 22540252). We would like to thank Drs. S. Mineshige, D. Nogami, A. Arai, K. Matsumoto, and S. Nakagawa for their comments and suggestions on this paper.

Appendix 1. Details of MCMC algorithm

We estimated $\{h\}$ by using the MCMC method. Here, we describe details of the MCMC algorithm and process to obtain $\{h\}$.

We used the multiple-try Metropolis (MTM) algorithm to sample the posterior probability distribution of our Bayesian model (Liu et al. 2000). The MTM algorithm is a modified Metropolis-Hastings algorithm, allowing larger step sizes with a reasonable acceptance rate. The dimension of our model is equal to the number of the cross-points of grids, namely $N = N_\theta(N_r + 1)$. In the main text, we set $N_r = 16$ and $N_\theta = 20$, hence $N = 340$. The MTM algorithm has an advantage in high dimension problems. We used the MTM algorithm because it gives convergence with a reasonable amount of computer time, while the standard Metropolis-Hastings algorithm does not.

We describe the procedure used to make the next set of h ($= \mathbf{y}$) from a given set of h ($= \mathbf{x}$) in the MTM algorithm in our model: 1) Draw k trial proposals, $\mathbf{y}_1, \dots, \mathbf{y}_k$ from

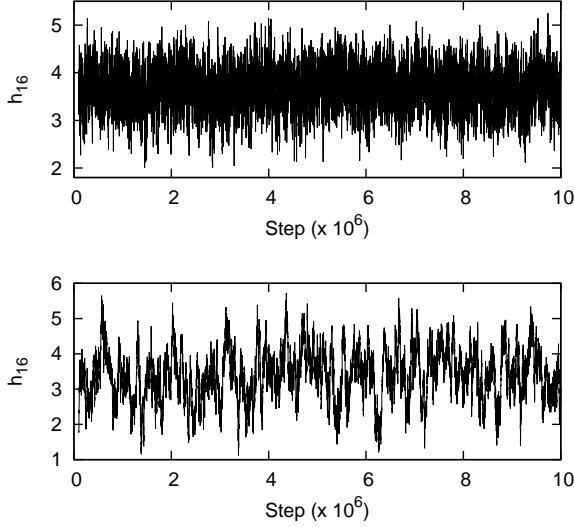


Fig. 15. Traces of a height parameter in the MCMC run. The calculations were performed with the same parameter as the case of Day 5 (see, table 1) with $w = 1.0$ in the upper panel and 2.0 in the lower panel.

a proposal distribution, $Q(\mathbf{x}, \cdot)$. 2) Select \mathbf{y} among the trial set $\{\mathbf{y}_1, \dots, \mathbf{y}_k\}$ with probability proportional to the posterior probability density, $P(\mathbf{y}_i)$ [see, equation (2)]. 3) Draw $\mathbf{x}_1, \dots, \mathbf{x}_{k-1}$ from $Q(\mathbf{y}, \cdot)$, and set $\mathbf{x}_k = \mathbf{x}$. 4) Accept \mathbf{y} with probability,

$$p = \min \left(1, \frac{P(\mathbf{y}_1) + \dots + P(\mathbf{y}_k)}{P(\mathbf{x}_1) + \dots + P(\mathbf{x}_k)} \right), \quad (\text{A1})$$

and reject it with probability $1 - p$. In the present study, we set $k = 5$. The proposal distribution $Q(\mathbf{y}, \mathbf{x})$ is a multivariate normal distribution with a mean of \mathbf{x} and a covariance matrix of $s\Sigma$. We defined Σ as the covariance matrix of the probability distribution, π' , which is an approximated probability of the prior, π ; $\pi' = \pi_{\text{smooth}}\pi'_{\text{disk}}$, where π'_{disk} is π_{disk} in $h > 0$ [see, equations (4) and (5)]. We control the step size by the scalar parameter, s . We update h of one quadrant of the disk in one step, and all h is updated in four steps. We choose s to achieve the acceptance rate of one step close to 0.1.

In all MCMC calculation presented in this paper, we discard the first 10^5 steps as a MCMC burn-in phase. All chains reached convergence after the burn-in phase. An example can be seen in the upper panel of figure 15, which shows the traces of a height parameter, $h_{16} = h(0.49, 0.00)$ in the MCMC run in subsection 3.2. We performed 10^7 steps and made the height map. We confirmed that there was no significant difference among the reconstructed height maps made from sub-samples of 10^6 steps. Figure 16 shows the posterior probability density function of h_{16} . The distribution has a single peak, and there is no evidence of other peaks. The form of the distribution indicates that the solution of the height map is uniquely determined.

All calculations in the present paper were performed

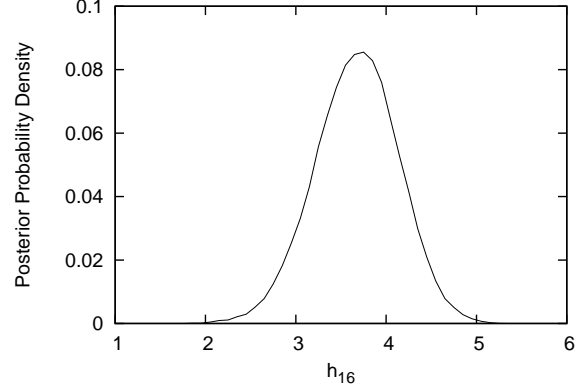


Fig. 16. Posterior probability density function of one of height parameters, h_{16} .

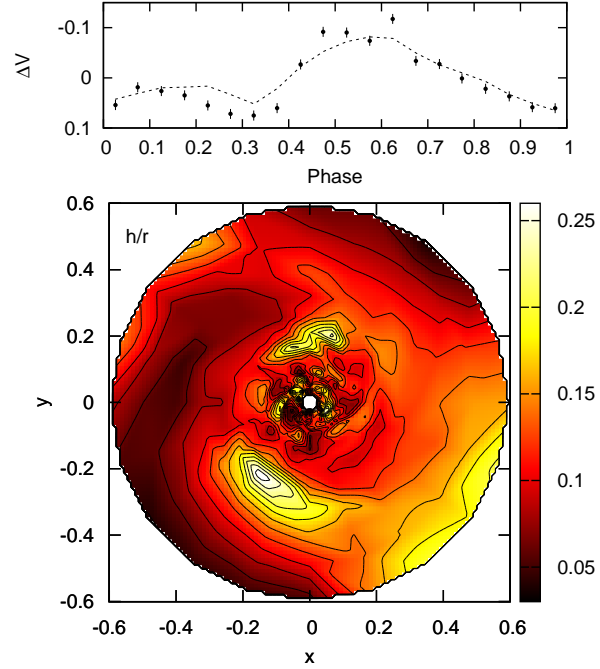


Fig. 17. Light curve (upper) and height map (lower) calculated with $w = 2.0$ using the data on Day 5 of V455 And. In the upper panel, the filled circles represent the observed light curves. The dashed line indicates the model light curve. The color maps and contours represent h/r . The contours are shown from $h/r = 0.00$ – 0.26 with an interval of 0.02. The secondary star is located at $(x, y) = (1.0, 0.0)$.

with $w = 1.0$. The trace of h_{16} calculated with $w = 2.0$ is shown in the lower panel of figure 15. In this case, it takes > 10 times longer than the case of $w = 1.0$ until convergence. Furthermore, the MCMC mixing is slow, as can be seen in figure 15. As a result, in order to obtain the final result, the amount of calculations with $w = 2.0$ is much larger than that with $w = 1.0$, and was impractical for the present study. It is an issue of computational time. It is noteworthy that, even with $w = 2.0$, the global pattern of the reconstructed height maps is consistent with that reported in section 3. Figure 17 shows the results calculated with $w = 2.0$: the model light curve (upper panel) and the reconstructed h/r map (lower panel). They were obtained from the last 5×10^6 steps in the lower panel of figure 15. The outermost and inner arm-like flaring patterns can be seen in the h/r map in figure 17, as seen in the case with $w = 1.0$ (figure 6). The flaring regions in figure 17 tend to be more localized than those in figure 6, as expected from the higher w . It indicates that a high w plays a role in increasing the resolution of the reconstructed height map, while the global structure of the map remains. In the main text, we used $w = 1.0$ because we have focused not on sub-structures, but on the global deforming-pattern of the disk.

References

- Araujo-Betancor, S., Gänsicke, B. T., Hagen, H.-J., Marsh, T. R., Harlaftis, E. T., Thorstensen, J., Fried, R. E., Schmeer, P., & Engels, D. 2005, *A&A*, 430, 629
- Dmitrienko, E. S. 2011, *Ap&SS*, 288
- Hachisu, I. & Kato, M. 2001, *ApJ*, 558, 323
- Horne, K. 1985, *MNRAS*, 213, 129
- Ishioka, R., Uemura, M., Matsumoto, K., Ohashi, H., Kato, T., Masi, G., Novak, R., Pietz, J., et al. 2002, *A&A*, 381, L41
- Kato, S., Fukue, J., & Mineshige, S. 2008, *Black-Hole Accretion Disks — Towards a New Paradigm —* (Kyoto: Kyoto University Press)
- Kato, T. 2002, *PASJ*, 54, L11
- Kato, T., Imada, A., Uemura, M., Nogami, D., Maehara, H., Ishioka, R., Baba, H., Matsumoto, K., et al. 2009, *PASJ*, 61, S395
- Kato, T., Nogami, D., Baba, H., Matsumoto, K., Arimoto, J., Tanabe, K., & Ishikawa, K. 1996, *PASJ*, 48, L21
- Kunze, S. 2004, *RevMexAA Conf. Ser.*, 20, 130
- Kunze, S. & Speith, R. 2005, in *The Astrophysics of Cataclysmic Variables and Related Objects*, ed. J.-M. Hameury & J.-P. Lasota Vol. 330 of *Astronomical Society of the Pacific Conference Series* (San Francisco: ASP), 389
- Liu, J. S., Liang, F., & Wong, W. H. 2000, *Journal of the American Statistical Association*, 95, 121
- Long, K. S., Mauche, C. W., Raymond, J. C., Szkody, P., & Mattei, J. A. 1996, *ApJ*, 469, 841
- Lubow, S. H. 1991, *ApJ*, 381, 259
- Maehara, H., Hachisu, I., & Nakajima, K. 2007, *PASJ*, 59, 227
- Marsh, T. R. & Horne, K. 1988, *MNRAS*, 235, 269
- Matsui, R., Uemura, M., Arai, A., Sasada, A., Ohsugi, T., Yamashita, T., Kawabata, K., Fukazawa, Y., et al. 2009, *PASJ*, 61, 1081
- Mauche, C. W. & Raymond, J. C. 2000, *ApJ*, 541, 924
- Nogami, D., Kato, T., Baba, H., Matsumoto, K., Arimoto, J., Tanabe, K., & Ishikawa, K. 1997, *ApJ*, 490, 840
- Ogilvie, G. I. 2002, *MNRAS*, 330, 937
- Osaki, Y. 1995, *PASJ*, 47, 47
- Osaki, Y. & Meyer, F. 2002, *A&A*, 383, 574
- Provencal, J. L., Shipman, H. L., Hog, E., & Thejll, P. 1998, *ApJ*, 494, 759
- Shakura, N. I. & Syunyaev, R. A. 1973, *A&A*, 24, 337
- Smak, J. I. 2001, *Acta Astron.*, 51, 295
- van der Woerd, H. 1987, *Ap&SS*, 130, 225
- Vogt, N. 1980, *A&A*, 88, 66
- Warner, B. 1985, in *Interacting Binaries*, ed. P. P. Eggleton, & J. E. Pringle (Dordrecht: D. Reidel Publishing Company), 367
- Whitehurst, R. 1988, *MNRAS*, 232, 35